Molecular dynamics simulations of SiO₂ melt and glass: Ionic and covalent models

J. D. Kubicki,* A. C. Lasaga

Department of Geology and Geophysics, Yale University, New Haven, Connecticut 06511, U.S.A.

Abstract

Computer simulations using the molecular dynamics (MD) technique have been carried out on SiO₂ melt and glass ranging from 300 to 9000 K and 0 to 175 kbar. The MD simulations used two sets of interatomic potentials—a simple ionic model with Born-Mayer repulsion terms and a central-force-field covalent potential—both of which were derived from quantum mechanical calculations on molecular clusters. Thermodynamic, structural, and diffusion data were obtained from these model systems and compared to experimental values wherever possible.

The MD results indicate that earlier X-ray diffraction data may need to be re-interpreted with respect to the SiOSi angle distribution. Bond-length and bond-angle responses to pressure and temperature changes compare favorably with experimental and theoretical studies on the α-quartz structure. Ring-distribution analyses show that planar rings containing three silica tetrahedra are present in the simulated glass. Predictions of second-order thermodynamic properties of the system (C_V, α, β) reveal inadequacies in the ionic approximation when applied to vitreous silica.

Arrhenius plots of ln D vs. temperature and pressure between 2000 and 6000 K and between 0 and 200 kbar show that at 6000 K, D increases with pressure from 1.3×10^{-5} at 40 kbar to 6.1×10^{-5} cm²/s at 100 kbar, then decreases to 1.5×10^{-5} at 175 kbar. Detailed analysis of the diffusion mechanism at pressures less than 100 kbar indicates that it is defect-controlled with high correlations between the percentages of 3- and 5-fold silicons, nonbridging oxygens, and the diffusion rate.

Introduction

In order to understand diffusion, nucleation, and crystal-growth kinetics in molten systems in an integrated way, an atomistic picture of the melt structure and its dynamics is necessary. Spectroscopic studies of silicate glasses have increased our knowledge of the structures that dominate these melts, but do not give much information about reaction mechanisms. With the molecular dynamics (MD) method, it has become possible to follow the motion of individual ions in a theoretical system and to determine both melt structure and reaction mechanisms in the molten state over a wide range of pressure and temperature.

An underlying concept behind our approach to these problems is that interatomic potentials in condensed phases are dominated by the same short-range forces present in isolated molecules (Newton and Gibbs, 1980; Newton et al., 1980; Gibbs, 1982). Thus, it is possible to translate data from quantum mechanical calculations on molecular clusters, such as H₄SiO₄ and H₆Si₂O₇, to interaction potentials between Si and O in silicate minerals and melts. Using this approach, it will be possible to put the understanding of melt dynamics into a firm theoret-ical framework that is simple and flexible enough to encompass many systems of geochemical interest.

In this paper, two potential-energy models derived from quantum mechanical calculations are applied to SiO₂ melts and glasses and used to extract thermodynamic, structural, and diffusion data. Shortcomings of using the ionic approximation to simulate covalent systems are exposed, but the utility of the MD technique in kinetic studies also becomes obvious, because diffusion mechanisms for Si and O can be displayed using computer graphics. Preliminary simulations with a covalent potential are also compared to the more extensive ionic results in an effort to increase the accuracy of model calculations. Inclusion of these short-range and many-body forces should make simulations more realistic for silica-rich melts.

Molecular dynamics

The MD calculation technique uses a central box containing at least a few hundred ions to simulate a melt or glass. A periodic boundary condition repeats this cell on all sides to create an infinite volume and remove surface effects. Within the central box, each ion interacts via short-range forces with all other ions up to a radius of 5 to 6 Å (except for the longer-range Coulomb force). In this study, the central box was subdivided into many smaller boxes (usually 64), and ions were assigned to one of the

---

* Present address: Geophysical Laboratory, Carnegie Institution of Washington, 2801 Upton Street, N.W., Washington, D.C. 20008, U.S.A.

small boxes. This technique reduces by several-fold the time involved in carrying summations over both short-range and Coulomb forces. The force on each ion is obtained by differentiating the computed interatomic potential energy for every ion:

$$F_i = \sum -(d\Phi_{ij}/dr_{ij})(dr_{ij}/du_i) \qquad (1)$$

where F_i = force on ion i in the u direction ($u = x, y, z$), Φ_{ij} = potential energy between ions i and j, r_{ij} = the distance between ions i and j, and du = the x, y, or z component of ion i. The sum in Equation 1 is over all j ions including those in the periodic boxes.

For the ionic model, Coulomb potential energies (Φ) are calculated at each time step by application of the Ewald technique to achieve efficient convergence (Sangster and Dixon, 1976):

$$\Phi = \frac{1}{2} \sum_i^N \sum_j^N \frac{Z_i Z_j}{r_{ij}} [\text{erf } c(\eta^{\frac{1}{2}} r_{ij})]$$
$$+ \frac{1}{2} \sum_i^N \frac{4\pi Z_i}{V_{\text{CELL}}} \sum_{G \neq 0}^\infty S(G) \left[\frac{\exp(-G^2/4\eta)}{G^2} \right]$$
$$- \sum_i^N Z_i^2 \left(\frac{\eta}{\pi} \right)^{\frac{1}{2}} \qquad (2)$$

where

$$S(G) = \sum_{t=1}^N Z_t \exp(-iG r_{it})$$

and the index i runs over all N ions in the cell, G is a reciprocal space vector, $S(G)$ is the structure factor, η is an arbitrary constant that can be chosen to speed up convergence (0.15 Å$^{-\frac{1}{2}}$ was used here), Z_i is the ionic charge of species i and V_{CELL} is the volume of the periodic box. The sum over reciprocal vectors in Equation 2 was carried out using the transformation introduced by Sangster and Dixon (1976), which decreases the time involved for each calculation by a factor of N, the number of ions. The potential in Equation 2 is also differentiated as in Equation 1 to add the Coulomb contribution to the total force on each ion.

Once the instantaneous force on each ion has been determined, its position and velocity are calculated for the next time step by using the algorithm of Schofield (1973):

$$r(t + \Delta t) = r(t) + v(t)\Delta t$$
$$+ \frac{1}{6}[4a(t) - a(t - \Delta t)]\Delta t^2 \qquad (3a)$$
$$v(t + \Delta t) = v(t)$$
$$+ \frac{1}{6}[2a(t + \Delta t)$$
$$+ 5a(t) - a(t - \Delta t)]\Delta t, \qquad (3b)$$

where $r(t)$, $v(t)$, and $a(t)$ are the position, velocity, and acceleration of an ion at time t. Accelerations are ob-

tained from the force on the ion by assuming that ions obey Newtonian mechanics ($\mathbf{F} = m\mathbf{a}$). The value of Δt in these simulations was 1.0×10^{-15} s at 4000 and 6000 K and 2.5×10^{-15} s at 2000 K.

All simulations were run on a cubic cell containing 324 ions (108 SiO₂ units). Runs were completed with initial temperatures ranging from 300 to 9000 K.

POTENTIALS USED IN THE MD SIMULATIONS

The most important factor in MD models is the accuracy of the potential equation that is chosen to simulate the forces between ions. One of the aims of this paper is to systematize the development of potential functions for use in MD simulations. Recently, Lasaga and Gibbs (1987) reported ab initio calculations of the Si-O potential and applied their results to the prediction of structural and elastic properties for the silica polymorphs α-quartz, α-cristobalite, and stishovite (the high-pressure polymorph). We propose to use these potentials, which have a firm theoretical basis and which have been tested on well-known mineral structures, in the MD simulations. In this fashion, we hope to remove some uncertainty from the interpretation of the MD results.

Most earlier work on silicates has used simple ionic potentials of the type

$$V_{ij} = \frac{Z_i Z_j e^2}{r_{ij}} + A_{ij}\exp(-r_{ij}/\rho_{ij}), \qquad (4)$$

where Z_i, A_{ij}, and ρ_{ij} could be varied to improve the comparison with experimental properties. The ionic potential used in this paper is a potential of the type given in Equation 4 but derived in Lasaga and Gibbs (1987) using ab initio results. The set of constants used for the ionic model (Table 1) are based on the usual formal charge $Z_{\text{Si}} = +4.0$, used in previous MD papers (e.g., Soules, 1979; Angell et al., 1982).

In this study, modeling of glasses and melts of the SiO₂ system was based not only on a simple ionic potential as in Equation 4 but also on a central-force-field covalent potential. The covalent parameters (Table 2) were derived from a Morse potential fit to ab initio quantum mechanical potential-energy surfaces (Lasaga and Gibbs, 1987). Based on these approximations for the Si-O interaction in the H₄SiO₄ and H₆Si₂O₇ molecules, calculations of the α-quartz structure using the WMIN program (Busing, 1981) gave good results for both the ionic and covalent potential models (Lasaga and Gibbs, 1987). However, only the covalent potential yielded a good equation of state and elastic constants.

The Lasaga and Gibbs data and methodology are used here; however, the form of the covalent potential is slightly modified for use in the MD simulations. The initial covalent potential chosen for the MD work was a combination of the Urey-Bradley force field and the flexible Morse potential:

TABLE 1. Ionic potential parameters

Z_{Si}	+4.0
Z_O	−2.0
A_{SiO} (eV)	1033.50
A_{OO} (eV)	914.20
ρ_{SiO} (Å)	0.32356
ρ_{OO} (Å)	0.33540

$$V = \sum_{SiO} D_{SiO}\{\exp[-2\alpha_{SiO}(r - r^0_{SiO})]$$
$$- 2\exp[-\alpha_{SiO}(r - r^0_{SiO})]\}$$
$$+ \sum_{OO} D_{OO}\{\exp[-2\alpha_{OO}(r - r^0_{OO})]$$
$$- 2\exp[-\alpha_{OO}(r - r^0_{OO})]\}$$
$$+ \sum_{SiSi} D_{SiSi}\{\exp[-2\alpha_{SiSi}(r - r^0_{SiSi})]$$
$$- 2\exp[-\alpha_{SiSi}(r - r^0_{SiSi})]\}$$
$$+ \sum_{i \neq j} \frac{Z_i Z_j e^2}{r_{ij}}. \qquad (5)$$

The second and third sums in Equation 5 are over pairs of atoms that are bonded to a common third atom. The r^0 parameters were obtained from the optimized STO-3G structure for $H_6Si_2O_7$ in Lasaga and Gibbs (1987) and are given in Table 2. The Morse parameters, D and α, as well as the effective charges, Z_i, were then obtained from a least-squares optimization of all the ab initio data in Lasaga and Gibbs (1987). These values are also given in Table 2. Note that the effective charge on Si is low (+0.4), as expected in a covalent model (Stewart et al., 1980). The bond strength of the SiO bond, as indicated by the large value of D_{SiO}, is higher than expected, reflecting a lack of adequate data for long bond lengths. Figure 1a gives the ab initio (Lasaga and Gibbs, 1987) contour potential surface as a function of SiO bond length and SiOSi angle for two linked SiO₄ tetrahedra. Figure 1b gives the contour surface as computed by the Morse potential in Equation 5. Figure 1c is a plot of the differences between Figures 1a and 1b. The Morse potential certainly reproduces the basic topology of the quantum mechanical results.

Figure 2a is a plot of the three Morse curves using the parameters in Table 2. Note the long tails of the potentials, which are a result of the weak 1–3 interactions. Figure 2b gives the ionic potential used for comparison. These Morse curves implicitly assume that the two Si-O atom pairs in either a SiOSi or an OSiO angle are "bonded." To use these Morse potentials in MD simulations, the bonding must be introduced in an efficient and smooth manner. This has been accomplished by modifying the Morse potential with a Fermi-Dirac–type term involving the two SiO bond lengths. This F-D-M potential is given by

$$V_{SiO} = \langle 1/\{\exp[\beta(r - r_l)] + 1\}\rangle V^{Morse}_{SiO} \qquad (6a)$$

$$V_{OO} = \langle 1/\{\exp[\beta(r - r_l)] + 1\}\rangle V^{Morse}_{OO} \qquad (6b)$$

$$V_{SiSi} = \langle 1/\{\exp[\beta(r - r_l)] + 1\}\rangle V^{Morse}_{SiSi} \qquad (6c)$$

TABLE 2. Morse potential parameters and Fermi-Dirac terms

	Si-O	O-O	Si-Si
D (kcal/mol)	563.4548	60.0980	121.4687
α (Å⁻¹)	0.8496	0.6192	0.6524
r^0 (Å)	1.6022	2.6531	3.0451
Z_{Si}	+0.4119		
β	30.0		
r_l	2.0		
SiO cutoff (Å)	2.3		

where r is the SiO bond distance in V_{SiO} and $r_l = \frac{1}{2}(r_{SiO1} + r_{SiO2})$ is the average SiO bond length in the V_{OO} and V_{SiSi} potentials. Table 2 gives the common set of β and r_l parameters. Figure 3 gives the modified F-D-M Si-O potential. Note that generally β and r_l are such that they do not perturb V_{ij} in the bonded region of usual interest ($r_{SiO} = 1.5$ to 1.7 Å). However, the F-D-M potential allows the possibility of bond breaking and bond forming to occur in glasses and melts.

Table 3 gives the structure and properties of α-quartz calculated from WMIN using the F-D-M potential. Generally, this potential does quite well and certainly much better than the purely ionic potential.

THERMODYNAMICS OF SiO₂ MELTS AND GLASSES FROM MD

The use of statistical mechanics and molecular dynamics has become a powerful method for determining thermodynamic properties of systems that are difficult to study experimentally. Application of MD to the study of geochemical systems has only begun in the past few years (Woodcock et al., 1976; Soules, 1979; Matsui and Kawamura, 1980; Matsui et al., 1981; Angell et al., 1982; Brawer, 1983; Mitra and Hockney, 1983; Dempsey and Kawamura, 1984); however, its utility and simplicity should make it a valuable and common tool in the future.

Primary data obtained in these simulations are the coordinates and velocities of each particle in the system as a function of time. Application of the theorems of statistical mechanics to this microcanonical ensemble (constant number of particles, volume, and energy) allows one to derive many thermodynamic properties such as heat capacities, thermal-expansion coefficients, and compressibilities. An important advantage of MD simulations is that the data can also be used to obtain kinetic information on the systems.

The total kinetic energy per unit cell is obtained from the velocities of the particles in the box

$$KE = \frac{1}{2}\sum_{i=1}^{N} m_i v_i^2, \qquad (7)$$

where N is the total number of particles in the cell, m_i is the atomic mass of the atom, and v_i is the velocity of atom i. The temperature of the system can then be computed by averaging the kinetic energy over many time steps ($N_{step} \geq 100$)

$$T = \frac{2}{3Nk}\langle(KE)\rangle = \frac{1}{3Nk}\left\langle\sum m_i v_i^2\right\rangle, \qquad (8)$$
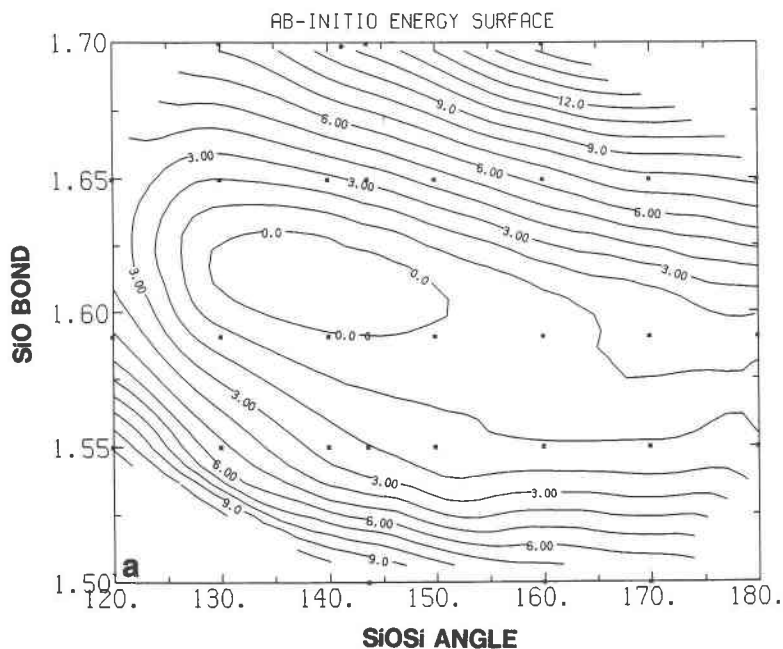
Fig. 1. (a) Quantum mechanical potential-energy surface for $H_6Si_2O_7$. The x axis is the SiOSi bond angle in degrees, and the y axis is the SiO bond length in Å. Energies are in kcal/mol. (b) Potential-energy surface for $H_6Si_2O_7$ calculated from Morse potential equation. (c) Energy differences between Figs. 1a and 1b test the ability of the Morse potential to reproduce quantum mechanical results.

where

$$\langle \cdots \rangle = \frac{1}{N_{step}} \sum_{steps} .$$

The temperature can also be set according to Equation 8 by scaling the velocities. Thus, if the desired value of the temperature is T_0 and the computed value according to Equation 8 is T, the velocities are scaled by

$$v_i^{new} = v_i^{old}(T_0/T)^{1/2}. \qquad (9)$$

Scaling is the MD equivalent of immersing the system in an isothermal heat bath.

In this study, the ions are initially positioned in a quartz-like structure that has been distorted to fit a cubic cell and then given a Boltzmann distribution of velocities for a chosen temperature. Since runs simulate real times of 1 to 2 ps (picoseconds), the initial temperature used to randomize the system is set at 10000 K (Angell et al., 1982) so that equilibrium is rapidly attained. Cooling is then done on successive runs in 1000-K increments.

The temperatures for each run were set by scaling particle velocities for 250 to 500 time steps. Another 1000 to 2000 steps were then calculated without temperature scaling. Cooling to the next temperature was then begun by scaling the velocities of the last time step from the previous simulation. Equilibration at each temperature was complete during scaling after 250 to 500 time steps as evidenced by the establishment of a well-defined thermodynamic average from the nonscaled temperature calculations. Numerical errors were checked by the conservation of total energy within the system (Figs. 4 and 5).

Both the potential energy (Eqs. 4 and 6) and kinetic energy (Eq. 7) will fluctuate around their average values, which should represent the bulk thermodynamic value for a macroscopic system. Figure 4 shows these fluctuations in kinetic energy, as represented by temperature, to be within 5% of the average. According to statistical mechanics theory (Hill, 1962), the standard deviation in temperature, $\Delta T/T_{avg}$, for a system with N particles is given by

$$\Delta T/T = \sigma \approx 1/(3N)^{1/2}. \qquad (10)$$

If $N = 324$, as in our system, Equation 10 predicts that the standard deviation, σ, should be approximately 6%, consistent with the results in Figure 4.

In these MD simulations, the total energy (E) of the system is constant after scaling has been removed. Therefore, fluctuations in the potential energy, Φ, and the kinetic energy, KE, must be coupled by the relation $E = \Phi + KE$. Figure 5 is a plot of the total energy as a function of time. Note that E varies by 0.1% due to numerical error, truncation of the power series in the Schofield algorithm, and approximation of the Ewald summation. We have assumed that this small error does not significantly affect our results.

Prediction of pressures in the system is problematic because the instantaneous pressure fluctuations within the system can be dramatic (e.g., instantaneous pressures may range from −100 to +100 kbar). Nonetheless, pressure estimates are made at each time step using the virial theorem (Woodcock, 1975)
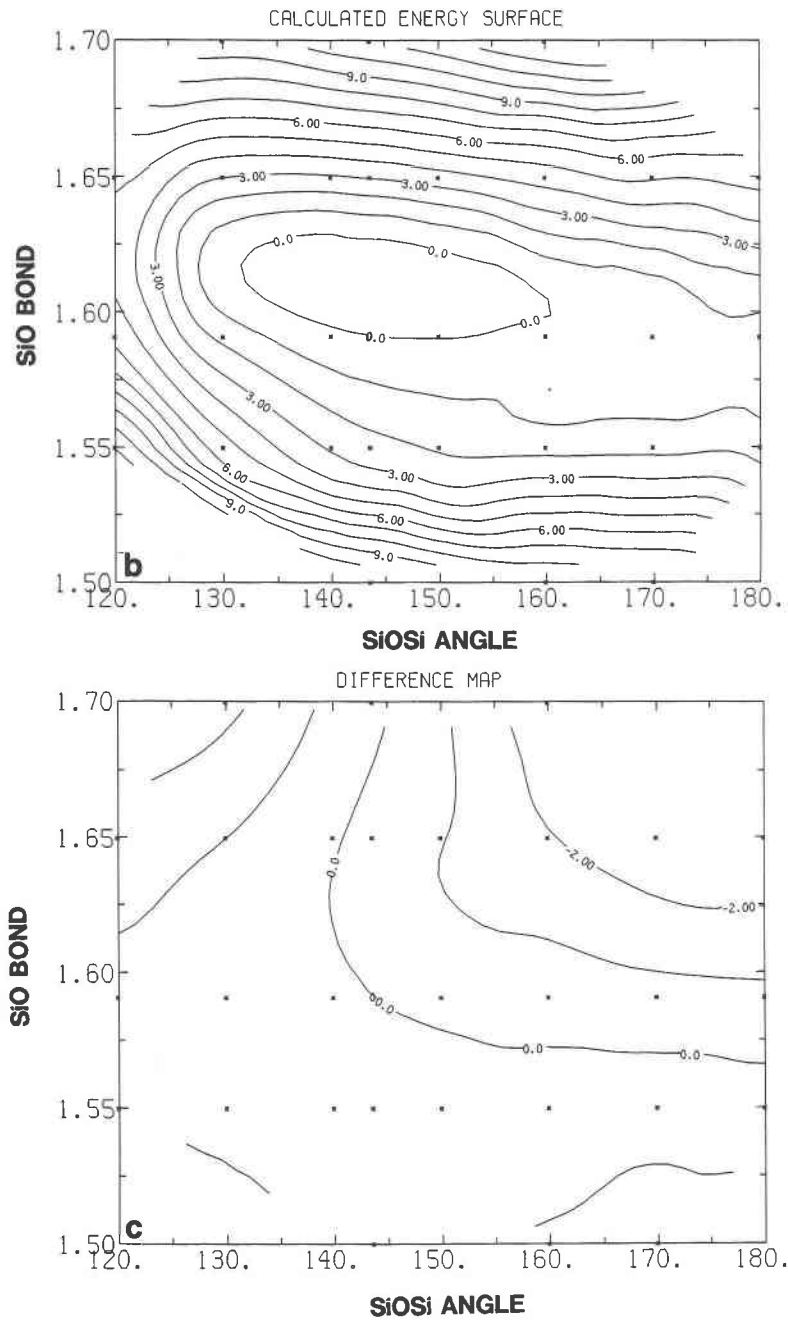
Fig. 1—*Continued.*

$$P = -(\partial A/\partial V)_T$$

$$= NkT/V + (1/3V)\left\langle \sum_{i=1}^{N} (\mathbf{r}_i \cdot \mathbf{F}_i) \right\rangle, \qquad (11)$$

where $\mathbf{F}_i$ is the force acting on ion i, $\mathbf{r}_i$ is the position vector, $(\partial A/\partial V)_T$ is the derivative of the Helmholtz free energy of the system with volume at constant temperature, and N and V are the number of ions and volume of the central box, respectively.

Values of the pressure are obtained by averaging over many time steps ($N_{step} \geq 100$). Figure 6 gives results of a typical run. Fluctuations of ± 10 kbar occur, but Figure 7 shows that a time-averaged pressure converges to a well-defined value. The simulations using the ionic potential, however, yield pressures that are substantially different from those predicted from the equation of state of SiO₂ glass at this temperature and density. This deviation (Table 4) stems from the difference between experiment and theory in the unit cell predicted with this potential in calculations on quartz (Lasaga and Gibbs, 1987). The simulations using the covalent potential predict pressures
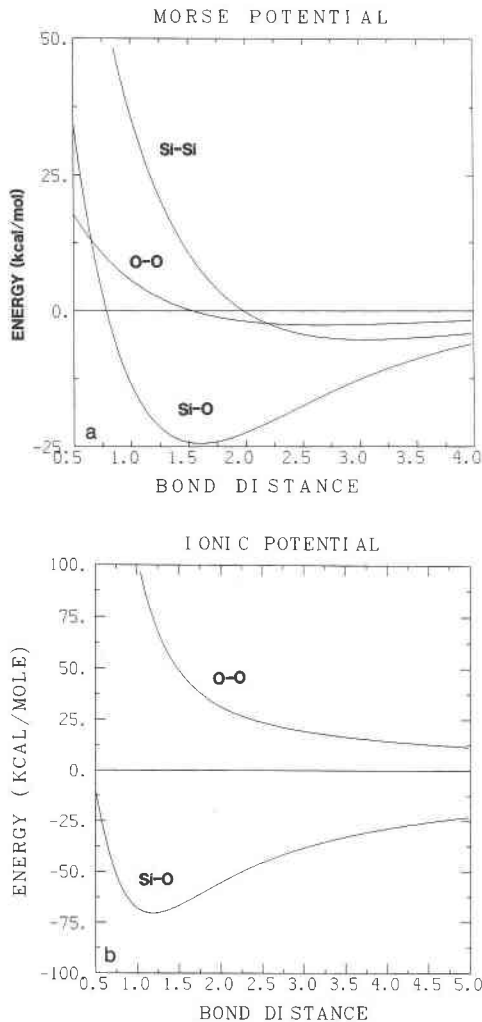
MORSE POTENTIAL

IONIC POTENTIAL

Fig. 2. (a) Interionic potential curves calculated for Si-O, O-O, and Si-Si interactions from the Morse potential equation with energies in kcal/mol vs. interionic distance in Å. (b) Potential curves calculated from the ionic potential equation.
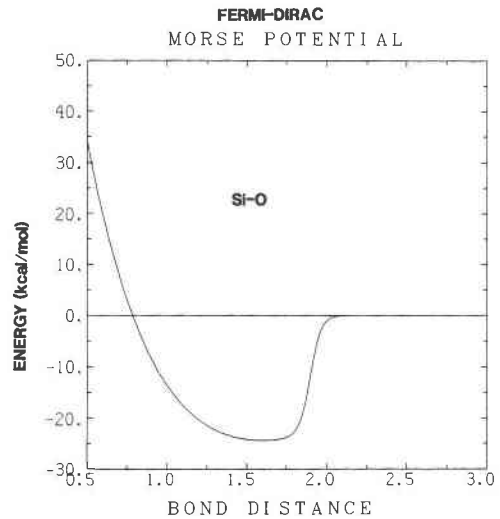

FERMI-DIRAC
MORSE POTENTIAL

Fig. 3. Si-O interaction potential calculated using the Fermi-Dirac-Morse potential. This plot is comparable to Fig. 2a for Si-O except for the F-D term, which limits the covalent bond to less than 2.3 Å.

where Φ = potential energy, k = Boltzmann's constant, and N_A is Avogadro's number. C_V values for SiO$_2$ glasses and melts predicted from MD and Equation 12 are given in Table 5 along with some experimental results for comparison. The agreement is very good at higher temperatures. This derivative property is a stringent test of the simulation and illustrates the usefulness of the ionic approximation in modeling silicate systems.

Thermal-expansion coefficients may be found using the thermodynamic relation $\alpha = (1/T)[1 - (1/V)(\Delta H/\Delta P)_T]$ in the form (Woodcock, 1975)

$$\frac{1}{V}\left(\frac{\partial V}{\partial T}\right) \equiv \alpha = \frac{1}{TV}\left[-\left(\frac{\partial E}{\partial P}\right)_T + P\left(\frac{\partial V}{\partial P}\right)_T\right], \quad (13)$$

using $H = E + PV$. In addition, isothermal compressibilities are calculated according to

that conform to experimental equations of state up to 10 kbar, again similar to the results obtained from static mineral calculations. These systems are under isostatic pressure as evidenced by the constancy of the center of mass throughout the run and by the equality of the $x, y,$ and z components of the pressure calculated individually (Fig. 8).

Fluctuations in first-order thermodynamic properties are not only required by the theorems of statistical mechanics, but they also allow calculation of higher-order thermodynamic properties. For example, changes in the potential energy within a given run are directly related to the constant-volume heat capacity by (Woodcock, 1975)

$$C_V = \frac{\langle\Phi^2\rangle - \langle\Phi\rangle^2}{kT^2} + \frac{3}{2}N_A k, \quad (12)$$

TABLE 3. Comparison of α-quartz structural parameters from experiment and from WMIN calculations using the Fermi-Dirac-Morse potential

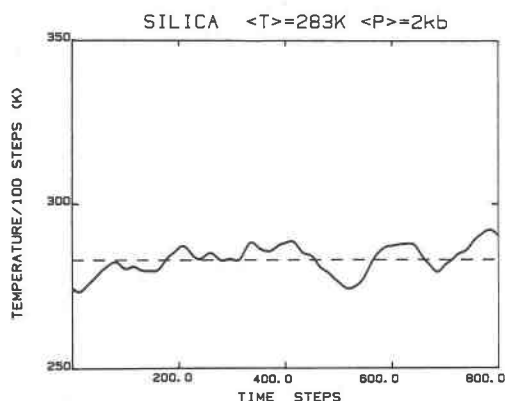|	Experiment	FDM potential
Unit cell		
a	4.9163	4.9286
c	5.4054	5.3456
Atomic position		
u	0.4697	0.4702
x	0.4135	0.4178
y	0.2669	0.2676
z	0.1191	0.1202
SiO1	1.6047	1.5997
SiO2	1.6137	1.5999
SiOSi (°)	143.7	145.0
β ($\times 10^{-6}$ bar^{-1})	2.54	3.35
$d\beta/dP$ ($\times 10^{-11}$ bar^{-2})		−1.8

Fig. 4. Variation in average temperature over 100 time-step intervals for a low-temperature, low-pressure silica glass using the ionic model. All scaled time steps of equilibration have been excluded.

$$\beta = -(1/V)(\partial V/\partial P)_T. \qquad (14)$$

Because these simulations use a microcanonical ensemble (constant N, V, and E), several runs with various volumes are used, and $(\partial V/\partial P)$ is calculated from the change in calculated average pressure with volume. Table 6 contains estimates for α and β of a SiO₂ melt from our simulations using the ionic model and experimental numbers for SiO₂ glass.

Prediction of second-order thermodynamic quantities is a stringent test of MD models, so the error in these predictions is encouragingly small. However, the more realistic covalent potentials are necessary for these simulations if accurate thermodynamic data are to be obtained.

STRUCTURE

Glass and melt structures can be analyzed using the pair correlation function
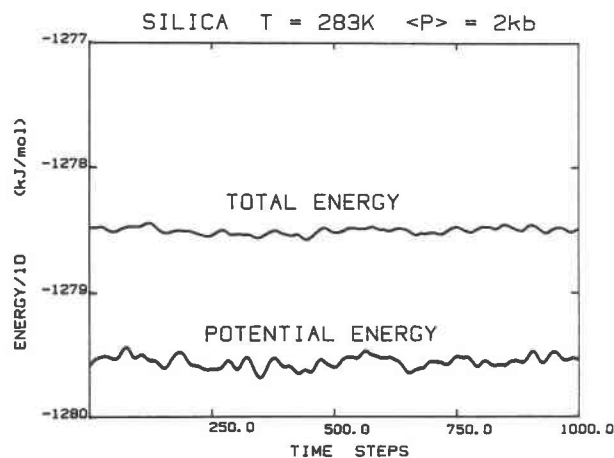

Fig. 5. Fluctuations of total and potential energies of the system over 1000 time steps after an initial equilibration period of 500 time steps using velocity scaling.
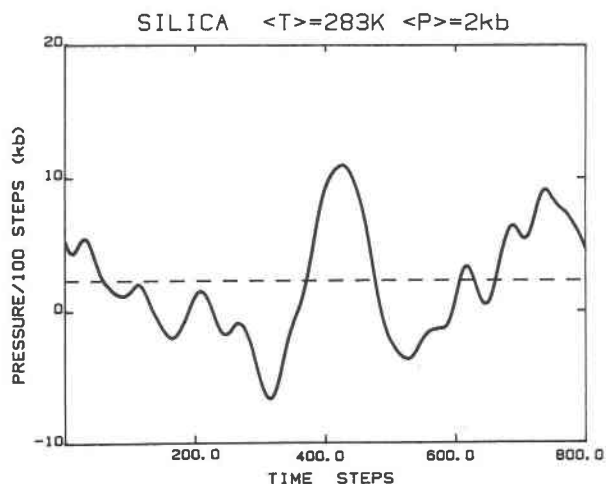

Fig. 6. Extreme calculated pressure variations are present even when averaged over 100 time steps for the simulation in Figs. 4 and 5. Temperature fluctuations do not control the pressure variations in this case because the NkT/V term of the virial theorem (Eq. 11) is very small at 300 K. The pressure predicted at this temperature and density from the SiO₂ glass equation of state is 0 kbar, and the average calculated pressure in this simulation is 2 ± 5 kbar.

$$g_{ij}(r) \equiv (1/4\pi\rho r^2)[dN(r)/dr] \qquad (15)$$

where $N(r)$ is the number of ions of type j within a sphere of radius r around a selected ion of type i, and ρ is the bulk density of the ions of type j. Note that as $r \to \infty$, short-range order and structure are lost, and $N(r) \to (4\pi/3)(\rho r^3)$. Therefore, $g_{ij} \to 1$ as $r \to \infty$. To calculate g_{ij} for these simulations, each ion is selected over 100 or more time steps, and the number of atoms of type j in thin spherical shells with radii of r and $r + \Delta r$ ($\Delta r = 0.025$ Å) around these ions [i.e., $dN(r)/dr$] are counted out to 10 Å. The correlation functions are averaged over the number of time steps and plotted to show the short-range melt structure. Figure 9 gives the results for the ionic model at the experimental density and 300 K as well as the curve determined from Mozzi and Warren's (1969) experimental data. Our fit to the experimentally derived correlation function is very good. The peaks disagree by 0.1 Å or less for primary coordination and by

TABLE 4. Cell dimensions, densities, and average calculated pressures for MD runs at 6000 K

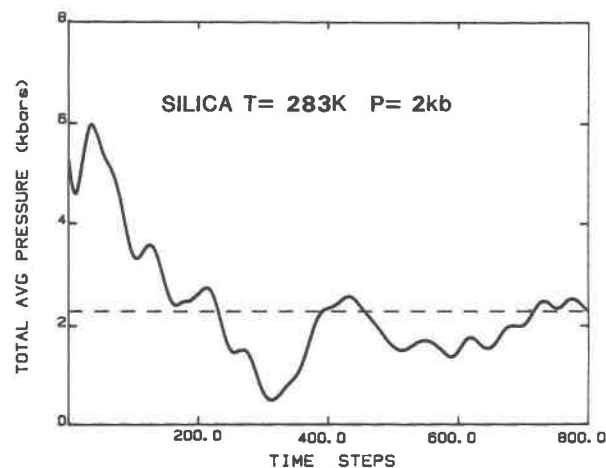| Cell length (L) (Å)	Density (ρ) (g/cm³)	Average calculated pressure (P) (kbar)
19.000	1.577	40
17.060	2.170	41
16.960	2.209	41
16.360	2.461	45
15.960	2.651	57
15.660	2.806	60
14.389	3.617	100
12.000	6.238	175

Fig. 7. Overall running average of the pressure plotted in Fig. 6. Convergence to a well-defined value indicates that the calculation is stable and that more realistic model potentials may allow accurate predictions of equations of state for glasses and melts.
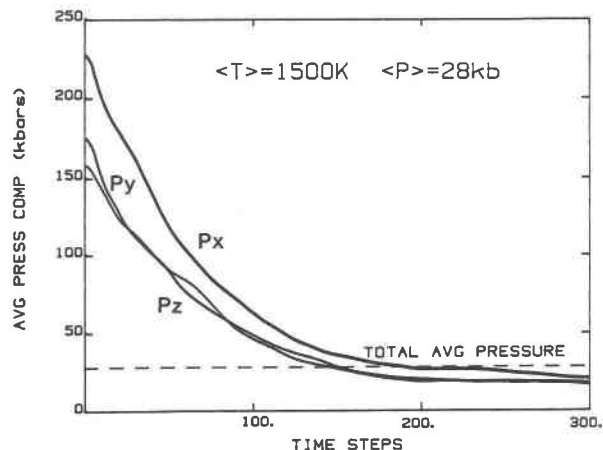

Fig. 8. Plot of running average for pressure components in the x, y, and z directions shows convergence toward the same value for all three components indicating isostatic equilibrium. Note that total average pressure is slightly higher than components because the (NkT/V) term of Eq. 11 is significant at the temperature of this simulation (i.e., 1500 K).

less than 0.5 Å for secondary coordination. This discrepancy is especially noticeable in the Si-Si correlation, and it is caused by the disagreement between the average SiOSi angle determined experimentally (144°) and the MD-calculated average SiOSi angle of these simulations (160°).

Coordination numbers (CN) are obtained by integrating to the first minimum, r_1, in the $g(r)$ curve.

$$CN = 4\pi\rho \int_0^{r_1} g(r)r^2 \, dr. \qquad (16)$$

Table 7 compares the values of first and second coordination numbers with experimental values found by Mozzi and Warren (1969) using X-ray diffraction. For primary coordination, the values in Table 7 are in good agreement with one another. The reason for the large errors in the secondary coordination numbers is unclear, but the breadths of the peaks in the correlation functions makes defining secondary coordination numbers ambiguous.

Coordination numbers may also be obtained by the location of plateaus in a plot of $N(r)$ vs. r (Fig. 10); the plateaus define the average number of ions clustered around each type of ion at a given distance. Primary coordination plateaus are very distinct, but there is diffi-

culty in defining secondary coordination because of the diffuse nature of the secondary coordination sphere in a melt or glass.

The average, primary polyhedral units are accurately reproduced by our models (Tables 7 and 8). However, the ionic approximation results in errors in the distribution of SiO bond lengths and OSiO angles (Fig. 11). The centers of the peaks for SiO and OSiO distributions are in the proper positions, but the widths of these peaks are broader than the widths of the experimentally derived peaks. For example, our SiO bonds vary by ±0.2 Å and OSiO tetrahedral angles by ±10°, whereas X-ray studies show a ±0.1 Å variance in SiO bonds (Mozzi and Warren, 1969) and ESR (Gaskell and Tarrant, 1980) experiments indicate a ±7° distribution around the average tetrahedral angle. Wide distributions are caused by the lack of directionality in the ionic potentials. Also, high-temperature structures may have been locked in by the very rapid cooling rates of MD simulations. The covalent model corrects this wide distribution for the SiO bond lengths, but the angle distribution remains unchanged (Fig. 11b).

The discrepancies for the value of the SiOSi angle have been a matter of controversy for some time. The original work of Mozzi and Warren (1969) was "corrected" by DaSilva et al. (1974) to give a value of 153.0°. Subsequently, however, Coombs et al. (1985) have vindicated the original work of Mozzi and Warren and re-calculated

TABLE 5. Comparison of MD-derived C_V and experimental C_P for SiO$_2$ at high temperatures

Temperature (K)	Density (g/cm³)	C_V (MD ionic) [J/(mol·K)]	C_P (experimental)* [J/(mol·K)]
300	2.209	70.73	37.94
1000	2.209	59.30	69.84
2000	2.209	66.98	79.90

* From Robie et al. (1978) except the 2000 K value, which has been extrapolated from their data.

TABLE 6. Isothermal compressibilities (β) and thermal-expansion coefficients (α) for SiO$_2$

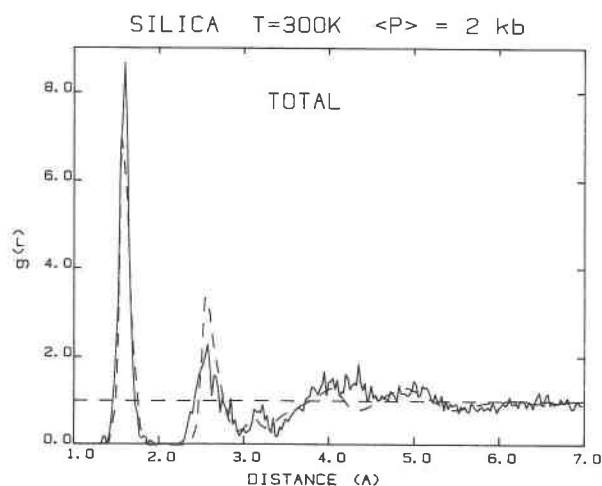| β (ionic MD) (bar⁻¹)	β (experimental) (bar⁻¹)	α (MD ionic) (K⁻¹)	α (experimental) (K⁻¹)
8.9×10^{-6}	2.45×10^{-6}	3.4×10^{-4}	0.5×10^{-6}

Fig. 9.   Calculated correlation function for silica glass from ionic MD model (solid line) and experimentally derived correlation function (dashed line; Mozzi and Warren, 1969). Positions of peaks, coordination numbers, and comparison to experimental values are given in Table 7.
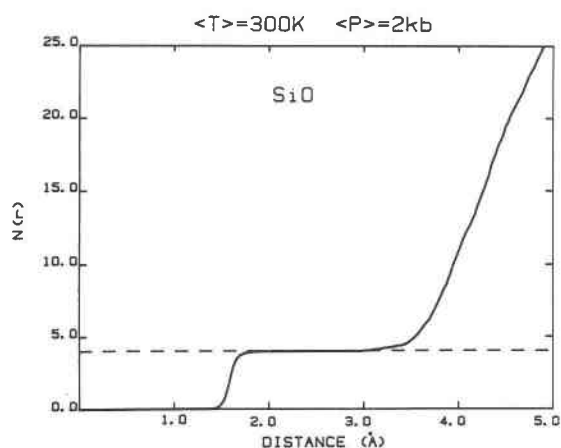

Fig. 10.   Number of O atoms with a radius of r, $N(r)$, vs. the distance from a given Si ion using the ionic model. Clear plateau at $N(r) = 4.0$ and $r = 2.0$ gives the coordination number of Si and a limit for the length of SiO bonds.

the average SiOSi angle at 144°. NMR spectroscopy (DuPree and Pettifer, 1984) has yielded a third SiOSi angle distribution, which is broader and more symmetric than that of Mozzi and Warren. Both this study and one by Mitra (1982) using MD on vitreous silica, however, predict average intertetrahedral bridging angles greater than 144° (160° and 153°, respectively). Both the low-T structure of quartz and quantum mechanical calculations on H$_6$Si$_2$O$_7$ dimers indicate that 140° should be the minimum-energy angle at 0 K (Fig. 1a). However, if this theoretical modeling is accurate, then the tendency should be for the SiOSi angle to expand with an input of thermal energy (Fig. 1a), and the average should be somewhat higher than 144° at temperatures not only above the melting point but even as low as several hundred degrees Celsius.

Analysis of ring geometries in our calculations using the ionic model (Table 9) reveals that the average SiOSi angle in rings containing 4 or more Si atoms is larger than 144°, as predicted by quantum mechanics, MD, and continuous random network (CRN) models (deLeeuw et al.,

1985). Since the vitreous SiO$_2$ structure is dominated by 5- and 6-membered Si rings (Table 10), it becomes difficult to justify the 144° average for the SiOSi angle from any theoretical evidence. These arguments do not preclude the original Mozzi and Warren (1969) statement that a maximum in the distribution occurs at 144°; however, this peak should be very broad and look more like the distribution obtained by DuPree and Pettifer (1984) using NMR spectroscopy. The only theoretical calculations we know of that reproduce the Mozzi and Warren distribution is the Gaskell and Tarrant (1980) computer-relaxed version of Bell and Dean's (1971) CRN model. Gaskell and Tarrant noted, however, that their model has overrelaxed the strain energy in the system by a factor of four and gives a bond-angle distribution that is too narrow (130° to 160° instead of 120° to 180°). As stated earlier, these tails on the intertetrahedral angle distribution are critical in determining the average because of the asymmetric slopes on the quantum mechanical potential-energy surface.

The ring statistics of the MD simulations are of interest as a comparison to other models and experiment. The results of our ionic, low-pressure model agree well with those of the MD model of Soules (1979) and the CRN

TABLE 7.   Comparison of coordination numbers (CN) and correlation function (15) peaks

Atomic pair	Coordination numbers			Correlation function peaks (Å)		
	Ionic	Covalent	Experiment	Ionic	Covalent	Experiment
SiO (I)	3.97	3.96	4	1.625	1.600	1.620
SiO (II)	28.3	20.8	12	4.300	4.300	4.15
OO (I)	5.85	6.46	6	2.55	2.525	2.65
OO (II)	46.6	22.9	18	5.100	5.125	4.95
SiSi (I)	3.92	4.20	4	3.200	3.200	3.12
SiSi (II)	21.2	9.7	12	4.600	5.650	5.18

Note: Values are from ionic and covalent MD results and from experiments of Mozzi and Warren (1969).

TABLE 8.   Comparison of average bond length and angles between ionic and covalent MD simulations and experiments

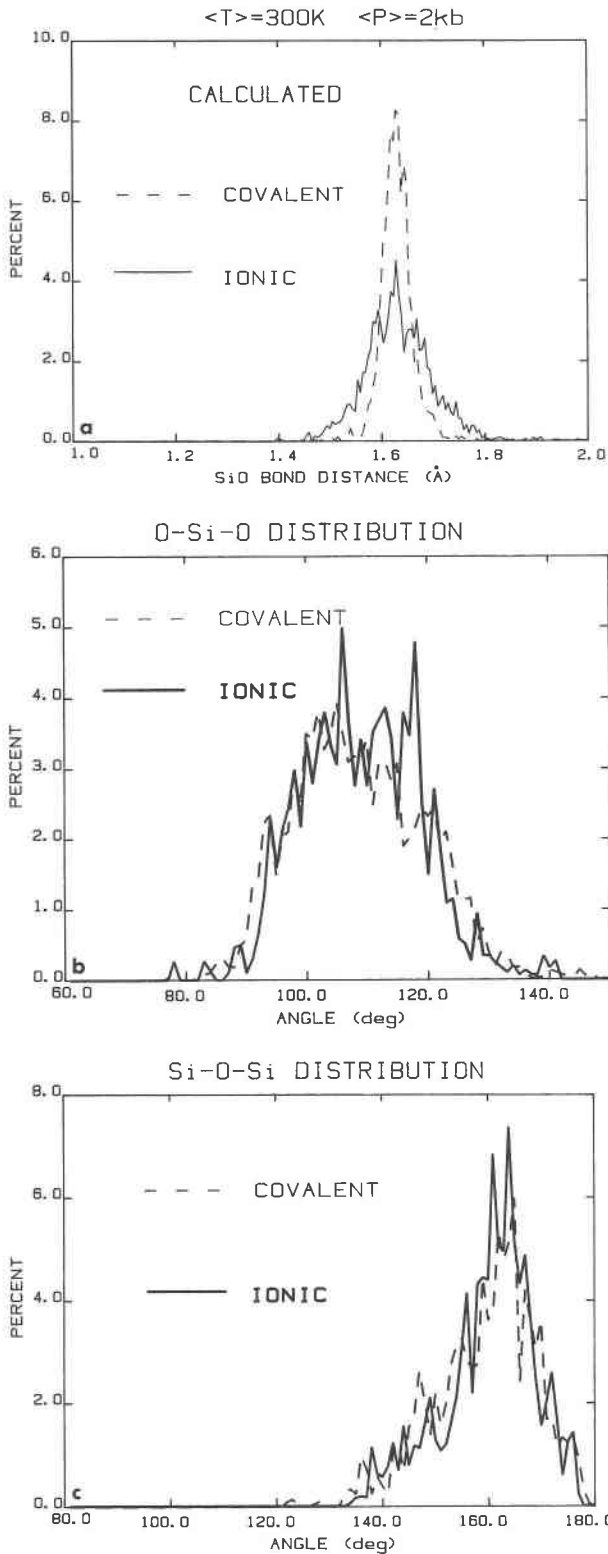|	SiO bond (Å)	SiOSi angle (°)	OSiO angle (°)
Ionic MD	1.642	160.5	108.9
Covalent MD	1.631	159.3	108.1
Experiment 1 (Mozzi and Warren, 1969)	1.620	144.0	109.5
Experiment 2 (DaSilva et al., 1974)	1.620	153.0	109.4

TABLE 9. Bond lengths and angles of rings in vitreous silica

SiO bond	OSiO angle	SiOSi angle
		Bulk average
1.638	108.9	160.6 (ionic MD)
1.631	108.1	159.3 (covalent MD)
1.636	109.1	152.7 (deLeeuw et al., 1985)
1.620	109.4	144.0 (Mozzi and Warren, 1969)
1.620	109.4	152.0 (DaSilva et al., 1974)
		Rings of three silica tetrahedra
1.643	108.0	140.4 (ionic MD)
1.668	89.8	129.5 (covalent MD)
1.636	100.6	132.0 (deLeeuw et al., 1985)
1.641	106.5	133.5 (STO6-31G*)
1.613	103.5	136.5 (analytic)
		Rings of four silica tetrahedra
1.633	108.7	159.1 (ionic MD)
1.617	106.3	154.4 (covalent MD)
1.636	105.1	146.4 (deLeeuw et al., 1985)
1.593	112.2	152.9 (analytic)

Note: The deLeeuw et al. (1985) values are from a continuous random network model (CRN). The STO6-31G* values are from high-level quantum mechanical calculations on isolated rings of three silica tetrahedra with nonbridging oxygens saturated with H atoms. Analytic values are from optimized ring structures in isolated molecular clusters based on equations fit to QM potential-energy surfaces.

model of Bell and Dean (1971) with the important exception of the existence of 3-membered Si rings in the MD models. These planar, highly strained structures have been used to explain the D_2 line in the Raman spectrum of SiO₂ glass (Galeener, 1982; McMillan et al., 1984). If this assignment is correct, the MD simulations may be a more accurate reproduction of glass structure than the ball-and-stick models. The ionic, high-pressure run (Table 10) shows that at $V/V_0 = 0.6$, 3- and 4-membered Si rings begin to dominate the structure of the glass. This finding supports the assignment of D_1 (Sharma et al., 1981) and D_2 to small rings on the basis of the intensity increases of these two peaks with pressure (Hemley et al., 1986). The change from 6-membered Si rings to 4-membered Si rings may also have some important effects on melt diffusion, as will be discussed later.

Given the above errors in the reproduction of the SiO₂ system, we have studied the changes of structure with temperature and pressure that are easily obtainable with MD. Compressibilities of individual bond types and angles are found from runs at different densities so that a "polyhedral" approach to studying the melt or glass may be adopted (Hazen and Finger, 1982). Knowledge of these factors is of great importance to the study of diffusion, nucleation, and crystal growth under geologic conditions where higher temperatures and pressures predominate.

Figure 12 shows the relative changes in three important structural features with pressure for the ionic model: SiO bond length, OSiO angle, and SiOSi angle. Clearly, the

Fig. 11. Plots of distribution of SiO bond lengths, OSiO tetrahedral angles, and SiOSi intertetrahedral angles with the ionic model results (solid lines) compared to the covalent model results (dashed lines). Actual distributions of tetrahedral angles from ESR experiments (Gaskell and Tarrant, 1980) and SiO bond

lengths from X-ray data (Mozzi and Warren, 1969) are narrower than the calculated distributions, but the covalent model significantly corrects the bond-length distribution as compared with the ionic model.

TABLE 10. Vitreous silica ring statistics

Ring size	Atoms in primary ring (%)	Model	Reference
2	0.0	MD	Soules (1979)
	0.0	CRN	Bell and Dean (1971)
	0.0	ILP	this study
	4.6	Covalent	this study
	5.6	IHP*	this study
3	5.0	MD	Soules (1979)
	0.0	CRN	Bell and Dean (1971)
	5.6	ILP	this study
	7.4	Covalent	this study
	12.0	IHP*	this study
4	11.0	MD	Soules (1979)
	19.0	CRN	Bell and Dean (1971)
	20.4	ILP	this study
	28.7	Covalent	this study
	50.0	IHP*	this study
5	24.0	MD	Soules (1979)
	28.0	CRN	Bell and Dean (1971)
	20.4	ILP	this study
	16.7	Covalent	this study
	23.1	IHP*	this study
6	61.0	MD	Soules (1979)
	53.0	CRN	Bell and Dean (1971)
	57.9	ILP	this study
	40.7	Covalent	this study
	8.3	IHP*	this study
7	1.9	ILP	this study
	1.9	Covalent	this study
	0.9	IHP*	this study

Note: MD = molecular dynamics; CRN = continuous random network; ILP = ionic, low-pressure; IHP = ionic, high-pressure.
* ρ = 3.617 g/cm³.

dominant effect of increasing pressure is the contraction of the SiOSi angle. As found in static calculations for quartz (Lasaga and Gibbs, 1987), most of the compressibility of SiO₂ is dependent upon this parameter. Tetrahedral angles and bond distances are much less compressible and do not undergo drastic change up to 100 kbar (Hazen and Finger, 1982), where Si changes to 6-fold coordination in stishovite. The [4]Si to [6]Si transition was observed in these simulations along with a consistent in-
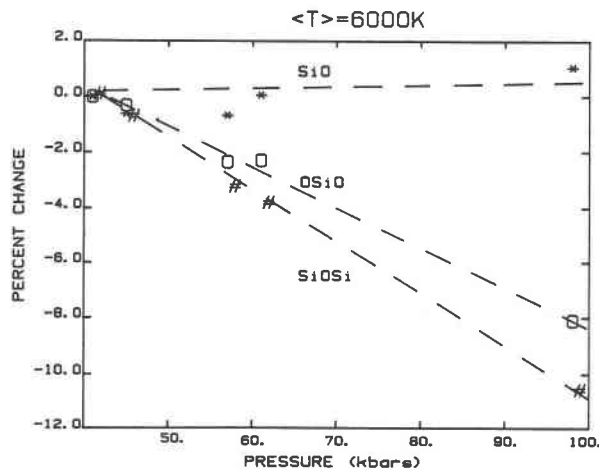

Fig. 12. Percent changes in average bond lengths and angles with pressure showing the relative flexibility of the SiOSi angle over SiO bonds and OSiO angles in the ionic model.
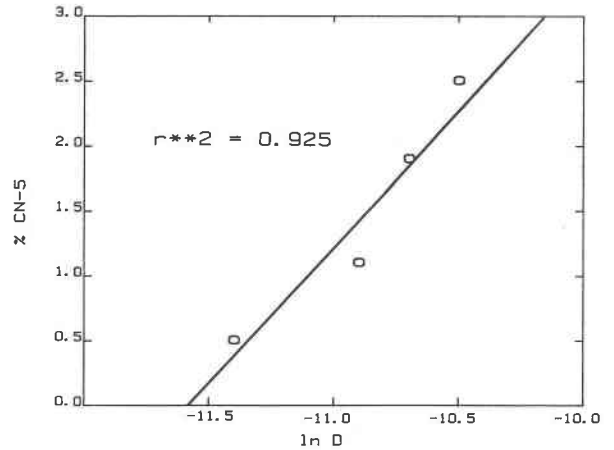

Fig. 13. This strong correlation between ln D_O (at 6000 K and 40 to 100 kbar) and 5-coordinated Si suggests that the anomalous increase in diffusion rate with pressure may be a defect-controlled process. The linear correlation coefficient here is 0.99.

crease in the percentage of [5]Si (Fig. 13). Contraction of the SiOSi angle should be expected in this simulation, because similar effects are seen experimentally in quartz under pressure. Levien et al. (1980) have shown that the SiOSi angle decreases by 6.5% and the SiO bond decreases by 0.26% when quartz is subjected to a pressure of 60 kbar. This is a change of −0.16°/kbar and −7 × 10⁻⁵ Å/kbar in quartz; our simulations give −0.09°/kbar and −18 × 10⁻⁵ Å/kbar over the same pressure range. Considering that the latter values are for a melt at 6000 K and the former are for crystalline quartz, this agreement is startling and may be an indication of the overall dominance of bulk properties such as compressibility by individual coordination polyhedra.

DIFFUSION

MD simulations allow calculation of self-diffusion coefficients by the Einstein equation

$$D = \frac{1}{6\tau N} \left\langle \sum_{i=1}^{N} [r_i(\tau) - r_i(0)]^2 \right\rangle \qquad (17)$$

where τ = time interval during diffusion, $[r_i(\tau) - r_i(0)]^2$ is the squared displacement of an ion of type i during the time interval τ, and N is the number of silicons or oxygens in the cubic cell. "$\langle \cdots \rangle$" in this case represents averaging over many different initial times. Equation 17 predicts a straight line for a plot of $\langle r^2 \rangle$ vs. time, and a slope that is related to the diffusion coefficient D_i. Given the time scale of MD simulations [1 ps (picosecond) = 1000 time steps = 75 h of CPU time on a VAX 11/750], diffusion coefficients are usually determined at geologically unreasonable temperatures (e.g., 6000 K). However, extrapolation of high-temperature values to more realistic conditions may be possible if the structure does not change drastically between the high- and low-temperature ends and there are no changes in diffusion mechanism across the extrapolated temperature range.
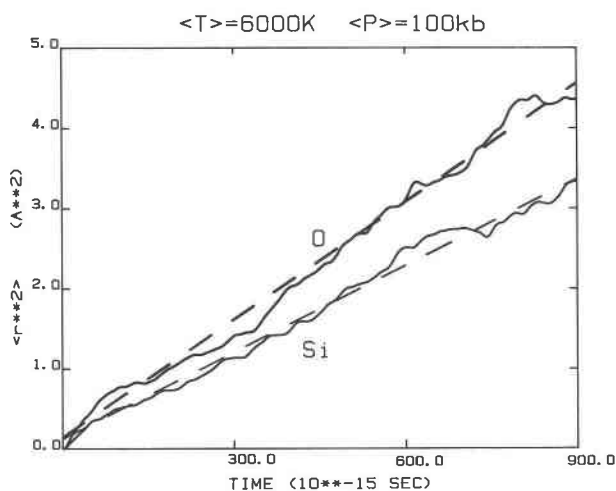
Fig. 14. Mean-squared displacement of O and Si at 6000 K and 100 kbar. Vibrations of atoms cause wiggles from best-fit line (dashed), and these become more significant at lower temperatures, which drastically increases the error in calculated diffusion coefficients at lower temperatures.

Fig. 16. The strong linear character of this ln D vs. pressure plot between 40 and 100 kbar allows for a fairly precise determination of activation volume for each atom type. Negative ΔV_a implies that strained species, such as 5-coordinated Si or 3-membered Si rings, may be controlling diffusion at high pressures.

Figure 14 is a plot of $\langle r^2 \rangle$ vs. time for O and Si at 6000 K and 100 kbar. The slope of the line is related to the diffusion coefficient by Equation 17. For O and Si, self-diffusion coefficients are 8.4×10^{-5} and 6.1×10^{-5} cm²/s, respectively, at 6000 K and 100 kbar; and both are approximately 2×10^{-5} at 6000 K and 40 kbar. These diffusion values are in reasonable agreement with theoretical values found for Si and O in alkali-silicate melts (5×10^{-5} cm²/s) by Soules (1979). Deviations from linearity increase in these plots as temperature decreases, probably because of the effects of vibrations imprinted on migration. Hence, at lower temperatures, the ions are
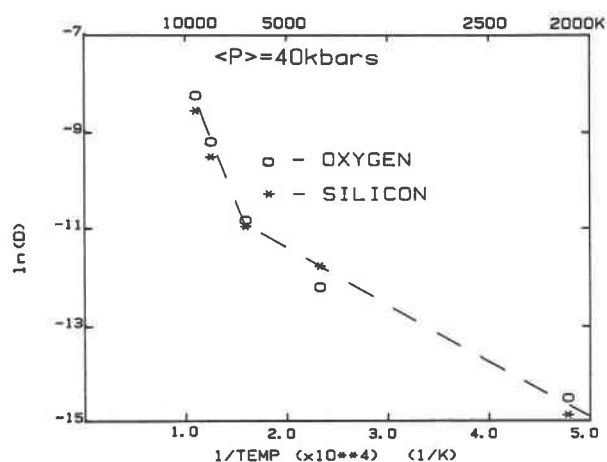
spending more time rattling around in their cages than moving through the melt, and longer run times are needed to obtain a reliable diffusion coefficient.

Runs of 1200 to 2000 time steps were made to investigate temperature and pressure variations of Si and O self-diffusion coefficients. Since the plots of mean square displacement (MSD) vs. time have an initial period where the relationship is parabolic and the Einstein equation (Eq. 17) does not apply, only the final 800 to 1000 time steps of each run were used to determine the diffusion coefficients [i.e., $t(0)$ was used as a starting configuration, but only $t(400)$ to $t(1200)$ were used to determine the slope of the line]. Using Arrhenius plots of ln D vs. $(1/T)$ and P (Figs. 15 and 16), activation energies and volumes may be determined from the relations

$$\ln(D) = (-\Delta E_a/R)(1/T) + \ln(A_1) \qquad (18)$$

for temperature changes and

$$\ln(D) = (\Delta V_a)(-P/RT) + \ln(A_2) \qquad (19)$$

for pressure changes. ΔE_a and ΔV_a are the activation energy and volume, respectively, R is the gas constant, and A is the y intercept of the least-squares fit line. Values obtained give a good check on the accuracy of the model when compared to experimental values, and they also give clues to the reaction mechanism involved in diffusion. Proposed mechanisms may then be verified with detailed molecular graphics of diffusing ions.

The ln D vs. $(1/T)$ plot shows a marked curvature indicating that the activation energy of diffusion is a function of temperature. If only the 2000 to 6000 K range is used, however, a linear trend is closely approximated (Fig. 15). Exclusion of the 8000 and 9000 K values is also justified by the large change in 2- and 3-coordinated silicons along with nonbonded oxygens at these temperatures. With the slope of the three lower-temperature

Fig. 15. Arrhenius plot of ln D vs. $1/T$ used to obtain activation energy of diffusion. Note large increase in ln D at $1/T = 1.6$ ($T = 6000$ K), which probably indicates a change of diffusion mechanism above this temperature that is associated with a large shift in melt structure toward 2- and 3-coordinated Si. Simulations at 2000 K were run for 2000 time steps with $dt = 2.5$ fs (femtoseconds).
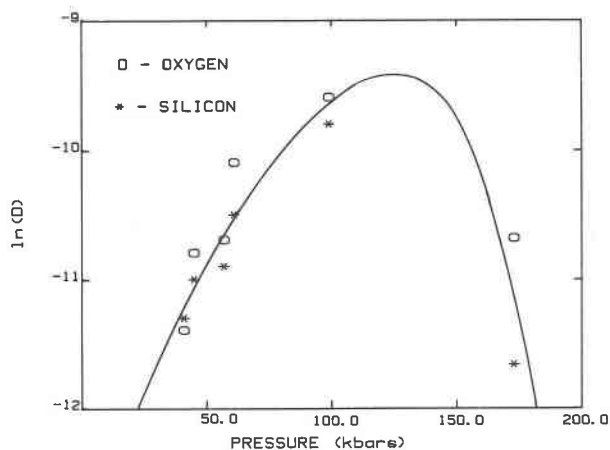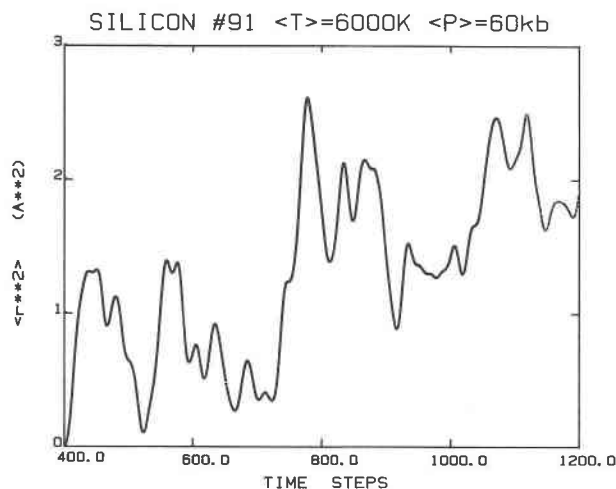
Fig. 17. Displacement squared of Si⁴⁺ ion after scaling has been removed for a simulation at $T = 6000$ K and $P = 60$ kbar. The rapid rise from $t = 550$ to $t = 600$ marks a diffusion event during which time the atom is also 3-coordinated (see Figs. 18 and 19).

points, the activation energies are 102.3 kJ/mol for Si and 91.1 kJ/mol for O. These values are low compared with experimental values of 200–400 kJ/mol. Both atom types are governed by similar energetics with the O moving more rapidly and diffusing more readily because of its lower mass and because it is not as tightly enclosed within its primary coordination sphere as Si.

Activation volumes are obtained from the slope of the ln D vs. pressure line (Fig. 16). Because the rate of diffusion increases with pressure up to 100 kbar, these ΔV_a values are negative, in agreement with experimental findings for other polymerized silicate melts (Kushiro, 1983). The activation volumes from the MD results are -4.01 cm³/mol for Si and -4.53 cm³/mol for O. The change in the diffusion rate for O with pressure is greater than for Si, which hints that the transition-state complex for diffusion is more compact for O than for Si, and both have denser structures than normal melt polyhedra. Thus, although temperature and pressure have opposite effects on the type of defects formed, the nature of SiO₂ melts causes both to increase the diffusion rate. Above 100 kbar, the diffusion coefficients decrease, because Si has become 6-coordinated and is more tightly bound within its primary coordination shell.

One of the biggest advantages that the MD technique enjoys is a knowledge of the positions of all individual ions as a function of time. Thus, reaction mechanisms may be checked directly with MD, and the ionic behavior should be as realistic as the potential used to model it. Figure 17 follows the displacement of a Si ion throughout a segment of a simulation. At time step 578, there is a large (≥ 1 Å²) displacement of this Si ion, and it begins to vibrate around an average position of 1.3 Å² compared to the average of 0.8 Å² before this step. This diffusion event coincides with step 578 in Figure 18, which shows that the Si ion is bonded to three oxygen atoms at this point. The structure of this complex is nearly trigonal
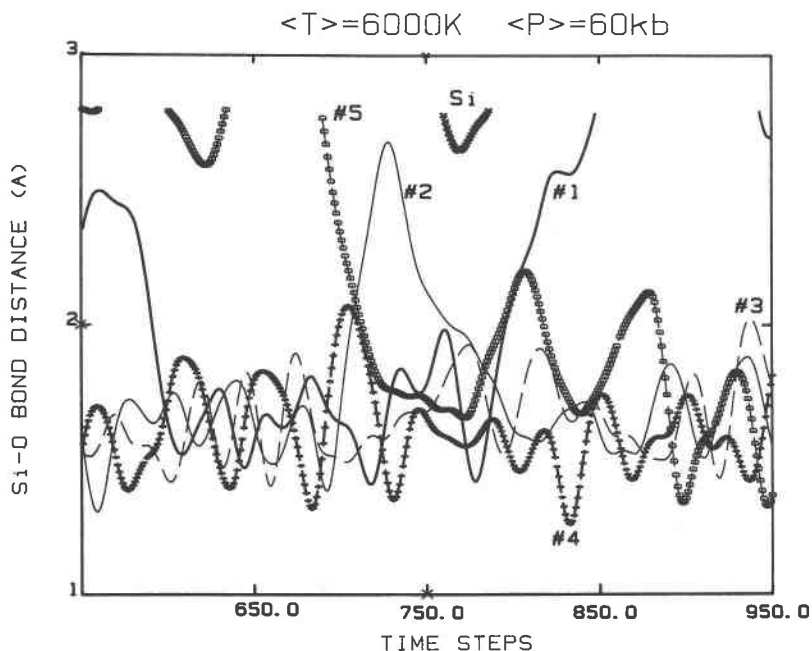

Fig. 18. Distances of nearest-neighbor O atoms to the Si atom of Fig. 17 plotted vs. time. The average SiO bond is 1.⌄→ Å in this case, and the maximum distance for a bond is set at 2.0 Å in these simulations. Note that the loss of no. 1 coincides with the return of no. 2 to a normal bridging O position. Also, no. 5 was a bridging O on a nearby tetrahedron that formed a 3-membered Si ring with the central Si atom before the loss of no. 1 occurred.
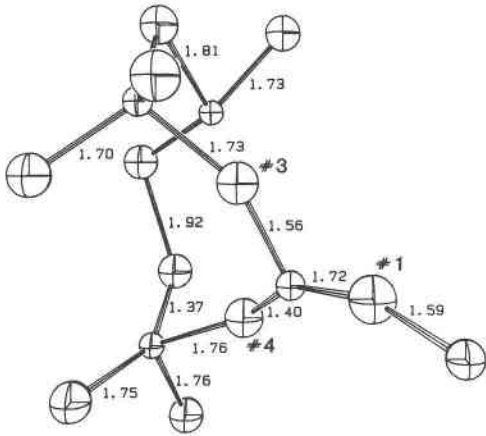
Fig. 19. Molecular graphics (ORTEP) of step 578 in Figs. 17 and 18. The formation of this trigonal planar complex coincides with a change in the average position of the central Si atom in the targeted tetrahedra. Bond distances are given in Å.

Fig. 21. Percentage of 3-coordinated Si and nonbridging oxygens are plotted vs. $\ln D$ (at $V = V_0$ and 2000 to 6000 K) here to illustrate the breakdown of polymerization and lowering of viscosity with increasing temperature. Correlations between these defects and $\ln D$ for Si and O are both 0.99, which is suggestive of a defect-controlled mechanism for diffusion.

planar (Fig. 19); the x coordinates of the Si and all three bonded oxygens are within ±0.5 Å of each other, and the OSiO angles are approximately 120°. Within this framework, it becomes possible to visualize Si diffusion normal to the equatorial oxygens toward the upper right of Figure 19.

At time step 700 in Figure 18, an O transfer begins between tetrahedra. As the new O becomes bonded to the central Si, a 5-fold complex is formed that is a distorted square pyramid (Fig. 20) corresponding to step 775 in Figure 18. A nearly planar ring with three silica tetrahedra is also formed at this time using the 5-fold Si. This highly strained complex brings another Si within 3 Å of
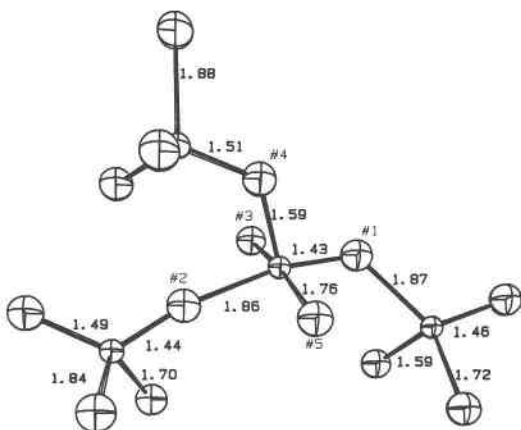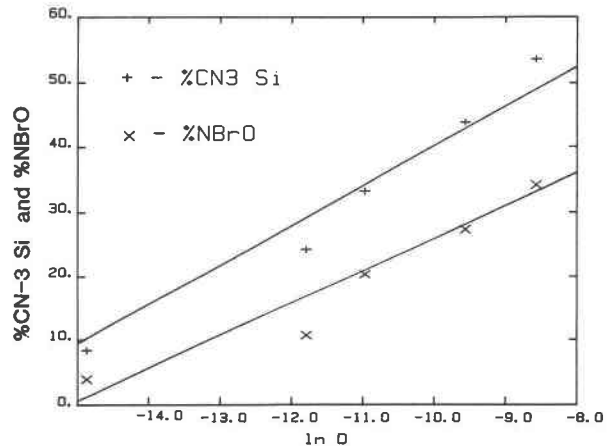

Fig. 20. Distorted square pyramidal complex from step 780 of Fig. 18 showing a mechanism of O transfer from one tetrahedron to another. No. 1 is the O leaving the original tetrahedron, and no. 5 is the new atom replacing it. All five of the oxygens bonded to the central Si are bridging oxygens, but two of the surrounding tetrahedra have been eliminated from the drawing for clarity.

the central Si atom and completes the oxygen transfer (Fig. 18). Within another 10 time steps, one of the originally bonded O atoms leaves the square pyramidal complex, and the central Si returns to a tetrahedral geometry without the 3-membered Si ring.

This mechanism involves a short-lived 5-coordinated Si that the pressure derivatives of the diffusion coefficients indicate may be a defect responsible for the anomalous pressure dependence of diffusion. Other workers (Brawer, 1981) have seen the effect of 5-fold coordination on diffusion in similar systems (BeF_2), and our data support this conclusion, because there is a strong correlation between the percentage of 5-fold Si and $\ln D$ in our data (Fig. 13). In addition, the increase of $\ln D$ with temperature is correlated with 3-coordinated Si and nonbridging oxygen species (Fig. 21).

The role of 3- and 4-membered Si rings in diffusion at high pressures is not clear but well worth investigating. If these strained species do play an active role in melt diffusion, they could explain the anomalous pressure dependence of diffusion coefficients for network-forming ions while at the same time slowing the diffusion rates of network-modifying cations. Computer animation of these simulations may be necessary to study many diffusion events and determine which structures are responsible for negative activation volumes in silicic melts and which are incidental.

At higher temperatures (i.e., $T \geq 6000$ K), different mechanisms apparently become the controlling factors for diffusion because the $\ln D$ vs. $(1/T)$ plot (Fig. 15) has a sharp increase in slope at this point and 3-fold Si and nonbridging O become abundant. Above 100 kbar, the 3-fold and 5-fold mechanisms are no longer applicable either, because there is a large decrease in the diffusion coefficient at this point and the transition to a melt dominated by 6-coordinated Si has taken place.

CONCLUSIONS

Molecular dynamics calculations using the ionic approximation have proven to be useful for molten salt systems but begin to become unrealistic for silicates in which the bonding has a substantially covalent character. Success in reproducing bonding geometries and diffusion properties with this method, however, is encouraging because its flexibility and simplicity allow new insight into previously intractable problems. Previously, mechanisms of diffusion and structures of melts at high pressures and temperatures had to be inferred from experimental results and were largely untestable. Further, the development of an integrated theory of melt diffusion, nucleation, and crystal growth may be possible with simulations of this type.

The most important development to be made now is a potential that will accurately describe the nature of the covalent bonding in silicates in order to more realistically model melt dynamics. The initial results using the covalent potential reported here encourage further work on refining such potentials. An important focus of future work will be spectral analysis of the MD simulations. Such work will be a stringent test on the accuracy of the models. It is our ultimate goal to be able to simulate known properties of silicates accurately enough (and without the use of empirically fit parameters) that faith may be put in extrapolations of thermodynamic and atomic properties into regions of P-T space not easily examined experimentally.

REFERENCES CITED

Angell, C.A., Cheeseman, P.A., and Tammaddon, S. (1982) Pressure enhancement of ion mobilities in liquid silicates from computer simulation studies to 800 kbars. Science, 218, 885–887.

Bell, R.J., and Dean, P. (1971) The structure of vitreous silica: Validity of the random network theory. Philosophical Magazine, 25, 1381–1398.

Brawer, S.A. (1981) Defects and fluorine diffusion in sodium fluoroberyllate glass: A molecular dynamics study. Journal of Chemical Physics, 25, 3516–3521.

——— (1983) Ab-initio calculation of the vibrational spectra of BeF₂ glass simulated by molecular dynamics. Journal of Chemical Physics, 79, 4539–4545.

Busing, W.R. (1981) WMIN. A computer program to model molecules and crystals in terms of potential energy functions. U.S. National Technical Information Service, ORNL-5747.

Coombs, P.G., DeNatale, J.F., Hood, P.J., McElfresh, D.K., Wortman, R.S., and Shackelford, J.F. (1985) The nature of the Si–O–Si bond angle distribution in vitreous silica. Philosophical Magazine B, 51, 39–42.

DaSilva, J.R.G., Pinatti, D.G., Anderson, C.E., and Rudee, M.L. (1974) A refinement of the structure of vitreous silica. Philosophical Magazine, 31, 713–717.

deLeeuw, S.W., He, H., and Thorpe, M.F. (1985) Vibrational spectra of rings in vitreous silica. Solid State Communications, 56, 343–346.

Dempsey, M.J., and Kawamura, K. (1984) Molecular dynamics simulation of the structure of aluminosilicate melts. Progress in experimental petrology. The Natural Environmental Research Council Publication Series D, No. 25, 49–55.

DuPree, E., and Pettifer, R.F. (1984) Determination of the Si–O–Si bond angle distribution in vitreous silica by magic angle spinning NMR. Nature, 308, 523–525.

Galeener, F.L. (1982) Planar rings in vitreous silica. Journal of Non-Crystalline Solids, 49, 53–62.

Gaskell, P.H., and Tarrant, I.D. (1980) Refinement of a random network model for vitreous SiO₂. Philosophical Magazine B, 42, 265–286.

Gibbs, G.V. (1982) Molecules as models for bonding in silicates. American Mineralogist, 67, 421–450.

Hazen, R.M., and Finger, L.W. (1982) Comparative crystal chemistry, 231 p. Wiley, New York.

Hemley, R.J., Mao, H.K., Bell, P.M., and Mysen, B.O. (1986) Raman spectroscopy of SiO₂ glass at high pressure. Physical Review Letters, 57, 747–750.

Hill, T.L. (1962) An introduction to statistical thermodynamics, 508 p. Addison-Wesley, New York.

Kushiro, I. (1983) Effect of pressure on the diffusivity of network-forming cations in melts of jadeitic compositions. Geochimica et Cosmochimica Acta, 47, 1415–1422.

Lasaga, A.C., and Gibbs, G.V. (1987) Applications of quantum mechanical potential surfaces to mineral physics calculations. Physics and Chemistry of Minerals, 14, 107–117.

Levien, L., Prewitt, C.T., and Weidner, D.J. (1980) Structure and elastic properties of quartz at pressure. American Mineralogist, 65, 920–930.

Matsui, Y., and Kawamura, K. (1980) Instantaneous structure of an MgSiO₃ melt simulated by molecular dynamics. Nature, 285, 648–649.

Matsui, Y., Kawamura, K., and Syono, Y. (1981) Molecular dynamics calculations applied to silicate systems: Molten and vitreous MgSiO₃ and Mg₂SiO₄. In S. Akimoto and M.H. Manghnani, Eds., High pressure research in geophysics, p. 511–524. Reidel, Boston.

McMillan, P., Piriou, B., and Couty, R. (1984) A Raman study of pressure-densified vitreous silica. Journal of Chemical Physics, 81, 4234–4236.

Mitra, S.K. (1982) Molecular dynamics simulation on silicon dioxide glass. Philosophical Magazine B, 45, 529–548.

Mitra, S.K., and Hockney, R.W. (1983) Molecular dynamics simulation of the structure of soda silica. Philosophical Magazine B, 48, 151–167.

Mozzi, R.L., and Warren, B.E. (1969) The structure of vitreous silica. Journal of Applied Crystallography, 2, 164–172.

Newton, M.D., and Gibbs, G.V. (1980) Ab-initio geometries and charge distributions for H₄SiO₄ and H₆Si₂O₇ compared with experimental values for silicates and siloxanes. Physics and Chemistry of Minerals, 6, 221–246.

Newton, M.D., O'Keefe, M., and Gibbs, G.V. (1980) Ab-initio calculation of interatomic force constants in H₆Si₂O₇ and the bulk modulus of α-quartz and α-cristobalite. Physics and Chemistry of Minerals, 6, 305–312.

Robie, R.A., Hemingway, B.S., and Fisher, J.R. (1978) Thermodynamic properties of minerals and related substances at 298.15 K and 1 bar (10⁵ Pa) pressure and higher temperatures. U.S. Geological Survey Bulletin 1452.

Sangster, M.J.L., and Dixon, M. (1976) Interatomic potentials in alkali halides and their use in simulations of the molten salts. Advances in Physics, 25, 247–342.

Schofield, P. (1973) Computer simulation studies of the liquid state. Computational Physics Communications, 5, 17–23.

Sharma, S.K., Mammone, J.F., and Nicol, M.F. (1981) Raman investigation of ring configurations in vitreous silica. Nature, 292, 140–141.

Soules, T.F. (1979) A molecular dynamics calculation of the structure of sodium silicate glasses. Journal of Chemical Physics, 71, 4570–4578.

Stewart, R.F., Whitehead, M.A., and Donnay, G. (1980) The ionicity of the Si–O bond in low-quartz. American Mineralogist, 65, 324–326.

Woodcock, L.V. (1975) Molecular dynamics calculations on molten ionic salts. In J. Braunstein, G. Mamantov, and G.P. Smith, Eds., Advances in molten salt chemistry, 3, 1–74.

Woodcock, L.V., Angell, C.A., and Cheeseman, P. (1976) Molecular dynamics studies of the vitreous state: Ionic systems and silica. Journal of Chemical Physics, 65, 1565–1567.